Biophysical Journal, Volume *114*

Supplemental Information

Forward and Reverse Waves: Modeling Distortion Products in the Intracochlear Fluid Pressure

Thomas Bowling and Julien Meaud

Supporting Material
Forward and reverse waves: modeling distortion products in the intracochlear fluid pressure
T. Bowling and J. Meaud

A Supplemental methods

A.1 Model Formulation

The mathematical model is formulated in the same manner as in our recent work [1], with the only difference being in how the middle ear is represented (here we only model the stapes, while a 2 degree-of-freedom model of the middle ear was used in Ref. [1]). As described in [2], the model includes degrees of the freedom for the acoustic fluid (the fluid pressure), the organ of Corti mechanics (at each section, it includes displacement degrees of the freedom for the BM and the TM) and electrical degrees of freedom (the electrical potential in the scala media, SV, ST and OHCs). Because the fluid is treated as inviscid and incompressible, the governing equation for the fluid is the Laplace equation ($\nabla^2 P = 0$); the governing equation for the organ of Corti is obtained from Lagrange's equations while the governing equations for the electrical degrees of freedom is obtained using Kirchoff's equation. The governing partial differential equations are transformed into the following system of ordinary differential equations using the finite element method:

$$\begin{pmatrix} \mathbf{M_s} & \mathbf{0} & \mathbf{0} \\ \mathbf{M_{sf}} & \mathbf{0} & \mathbf{0} \\ \mathbf{0} & \mathbf{0} & \mathbf{0} \end{pmatrix} \begin{pmatrix} \ddot{\mathbf{u}} \\ \ddot{\mathbf{p}} \\ \ddot{\phi} \end{pmatrix} + \begin{pmatrix} \mathbf{C_s} & \mathbf{0} & \mathbf{0} \\ \mathbf{0} & \mathbf{0} & \mathbf{0} \\ \mathbf{C_{es}} & \mathbf{0} & \mathbf{C_e} \end{pmatrix} \begin{pmatrix} \dot{\mathbf{u}} \\ \dot{\mathbf{p}} \\ \dot{\phi} \end{pmatrix} + \begin{pmatrix} \mathbf{K_s} & \mathbf{K_{fs}} & \mathbf{K_{se}} \\ \mathbf{0} & \mathbf{K_f} & \mathbf{0} \\ \mathbf{K_{es}^{lin}} & \mathbf{0} & \mathbf{K_e} \end{pmatrix} \begin{pmatrix} \mathbf{u} \\ \mathbf{p} \\ \phi \end{pmatrix} + \begin{pmatrix} \mathbf{0} \\ \mathbf{0} \\ \mathbf{F_{es}^{NL}(u)} \end{pmatrix} = \begin{pmatrix} \mathbf{F_u} \\ \mathbf{0} \\ \mathbf{0} \end{pmatrix} \quad \text{(S1)}$$

where $\mathbf{u}$ the vector of the structural displacements (with the displacement of the stapes as the first element), $\mathbf{p}$ is the vector of intracochlear fluid pressures, ϕ is the vector of electrical potentials, $\mathbf{F_{es}^{NL}}$ is a nonlinear term that arises due to nonlinearities in I_{MET} (see Refs. [3, 1] and Eq. 4 in the manuscript) , and $\mathbf{F_u} = [f(t), 0 \cdots 0]^T$ where $f(t)$ is the stimulus force applied on the stapes. The mechanical, acoustic, and electrical domains are coupled through the off-diagonal matrices on the left side of Eq. S1. In the linearized version of the model, $\mathbf{F_{es}^{NL}}$ is linearized while it is kept as a nonlinear term in the nonlinear version of the model. The process for formulating Eq. S1 in state space form is described in Ref. [1].

A.2 Model Parameters

Model parameters here have been adjusted from those of the guinea pig to represent the gerbil cochlea. Any model parameter not listed here is given in [2].

A.2.1 Geometrical parameters

The geometric parameters for the micromechanical model are shown in Table S1. A comparison of the anatomical model with images from Edge *et. al* [4] is shown in Figure S1.

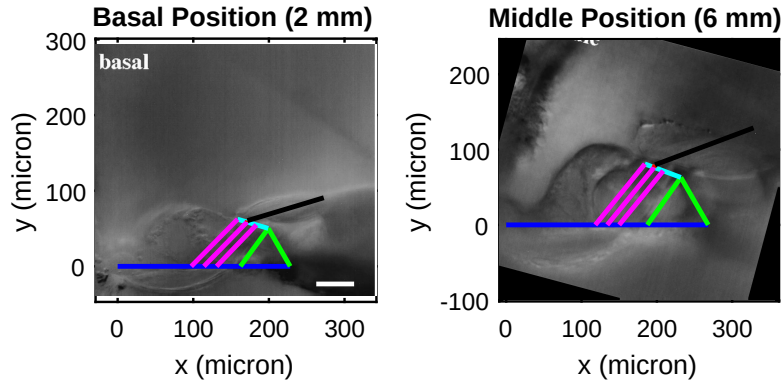

Figure S1: Geometrical model of the organ of Corti overlapped with images of the organ of Corti from [4] at a basal and middle turn location.

Table S1: Anatomical parameters for the model (x in cm).

Parameters	**Description**	**Value**
L	Length of BM	1.12 cm
L_h	Length of Helicotrema	0.1 cm
w	Width of cochlear ducts	0.1 cm
h	Height of each cochlear duct	0.1 cm
A_s	Cross-sectional area of stapes	$A_s = hw = 0.01$ cm^2
b	Width of BM	208μm (base) to 320μm (apex)
L_{tm}	Length of TM from pivot to middle HB	88μm (base) to 184μm (apex)
α	Angle between RL and BM	15° (base) to 26° (apex)
β	Angle between HB and vertical	15° (base) to 26° (apex)
L_0	Distance between left edge of BM and contact of middle OHC with BM	$b/2$
L_1	Radial distance between HBs	13 μm
L_{pc}	Distance between left edge of BM and contact of outer pillar cell	58μm (base) to 100μm (apex)
L_{hb}	Length of HBs	1μm (base) to 6μm (apex)
L_{ro}	Distance between RL pivot and middle OHC	25.1μm (base) to 49μm (apex)
θ_1	Angle between inner pillar cell and BM	60°
θ_2	Angle between inner and outer pillar cells	60°

A.2.2 Mechanical parameters

Cochlear model

Table S2: Mechanical parameters for the cochlear model (x in cm). Parameters denoted * are defined per unit length.

Parameters	Description	Value	Ref.
K_{bm}	BM stiffness *	$18.4\exp(-7.54x) \times 10^5$ N/m^2	assumed
D_{xx}	BM plate bending stiffness (xx) *	$10^{-10}\exp(-0.5x)$ N.m	[5]
D_{xy}	BM plate bending stiffness (xy) *	$10^{-10}\exp(-0.5x)$ N.m	[5]
D_{shear}	BM plate bending stiffness (shear) *	$4.3\exp(-0.5x) \times 10^{-11}$ N.m	[5]
K_{tms}	TM shear stiffness *	$2.31\exp(-1.32x^2 - 6.42x) \times 10^5$ N/m^2	assumed
K_{tmb}	TM bending stiffness *	$3.84\exp(-7.54x) \times 10^4$ N/m^2	assumed
K_{rl}	RL stiffness *	$2.78\exp(-7.54x) \times 10^3$ N/m^2	assumed
K_{ohc}	OHC stiffness *	$5.07\exp(-7.54x) \times 10^3$ N/m^2	assumed
K_{hb}	HB stiffness *	$291\exp(-7.54x)$ mN/m	assumed
M_{bm}	BM mass *	2.8×10^{-7} kg/m	[6]
M_{tms}	TM shear mass *	$3.58\exp(1.58x) \times 10^{-6}$ kg/m	based on [7, 8]
M_{tmb}	TM bending mass *	$1.12\exp(2.15x) \times 10^{-6}$ kg/m	based on [7, 8]
c_{bm}	BM damping coefficient *	8.5×10^{-2} N.s/m^2	assumed
c_{hb}	HB damping coefficient	$\eta_f \frac{L_{tm}}{3L_{hb}}$, where $\eta_f = 1.0 \times 10^{-3}$ N.s/m^2 is the viscosity of the fluid	[5]
c_{tmb}	TM bending damping coefficient *	0.1 N.s/m^2	assumed
c_{tms}	TM shearing damping coefficient *	3×10^{-3} N.s/m^2	assumed
G_{tms}	TM shear modulus	$7.0\exp(-3.75x)$ kPa	[8, 5]
η_{tms}	TM shear viscosity	0.03 Pa.s	[9], based on [10]
ρ_f	fluid density	1000 kg/m^3	

Middle ear model

When reverse fluid waves reach the stapes, some of the wave energy is transmitted through the middle ear

and out into the ear canal while the rest is reflected back towards the apex as a forward traveling wave. In the frequency domain, the reverse middle ear impedance (*i.e*, the impedance looking out from the stapes in the reverse direction [11]) is given by:

$$Z_{meR} = \frac{1}{A_s^2}\left[M_s i\omega + C_s + \frac{K_s}{i\omega}\right] \tag{S2}$$

where M_s, C_s and K_s are the mass, damping coefficient, and stiffness coefficient of the stapes, respectively; ω is the radian frequency and A_s is the area of the stapes footplate. The stapes reflection coefficient is given as [12]:

$$R_{st} = \frac{Z_{meR}/Z_c^* - 1}{Z_{meR}/Z_c + 1} \tag{S3}$$

where R_{st} is the stapes reflection coefficient, Z_c is the input impedance of the cochlear model, and * denotes the complex conjugate. The values of the stapes reflection coefficient, R_{st}, cochlear input impedance, Z_c, and reverse middle ear impedance, Z_{meR}, are presented in Fig. S2 Because there are no measurements of the middle ear reverse impedance or stapes reflection coefficient in the gerbil ear, the value of the middle ear parameters were chosen such that the reflection coefficient is similar to what has been reported in the human [11]. The mechanical parameters for the middle ear model are presented in Table S3. All results in the manuscript are obtained with the baseline model. In addition to the baseline model, models with small and large stapes reflection coefficient magnitudes, $|R_{st}|$, where developed. The effects of varying the magnitude of R_{st} on DP propagation are shown in Fig. S9.

Table S3: Mechanical parameters for the middle ear model.

Parameters	Description	Baseline	High $\lvert R_{st}\rvert$	Low $\lvert R_{st}\rvert$
M_s	Stapes mass (kg)	3.0×10^{-7}	3.0×10^{-7}	6.6×10^{-7}
C_s	Stapes damping coefficient (N.s/m)	6.0×10^{-2}	1.0×10^{-3}	3.4×10^{-1}
K_s	Stapes stiffness (N/m)	5.0×10^{2}	5.0×10^{2}	2.3×10^{4}

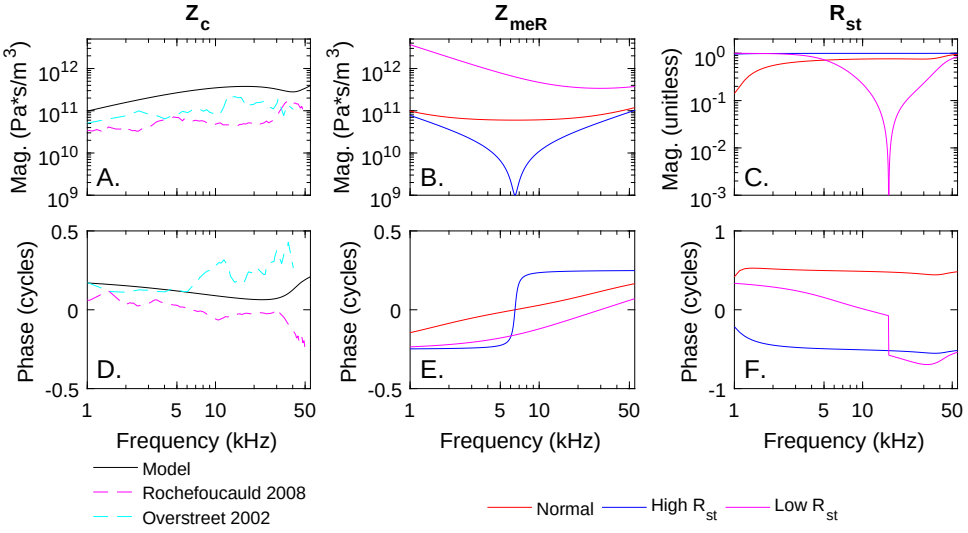

Figure S2: Different middle ear models. A. and D. Magnitude and phase of the cochlear input impedance, compared to data from [13, 14]. The model cochlear input impedance is computed by taking the ratio of the scala vestibuli pressure next to the stapes to the volume velocity of the stapes. B.,E. Magnitude and phase of the reverse impedance of the middle ear model. C.,F. Magnitude and phase of the stapes reflection coefficient.

A.2.3 Electrical parameters

The electrical parameters for the cochlear model are shown in Table S4. The value of the basolateral conductance and capacitance were set to the values reported in [15]. The HB saturating conductance, G_a^{max}, was chosen to be a free parameter whose value was varied during the calibration process to give BM gain values that matches the experimental data from [16, 17]. The value of the conductance is somewhat higher than the values reported by Johnson et al. [15] in the gerbil cochlea. As in [3], the constants ΔX and X_0 of Eq. 4 are given by

$$\Delta X = \frac{f_{gs}\gamma}{k_B T} \tag{S4}$$

$$X_0 = \Delta X \log(1/P_0^s - 1) \tag{S5}$$

where $f_{gs} = 10$ pN is the single channel gating force in the tip link direction, $\gamma = 0.5\mu\text{m}/L_{hb}$ is the geometrical gain factor, k_B is the Boltzmann constant, $T = 37°C$ is the temperature, and P_0^s is the resting probability of the MET channel (assumed to be equal to 0.4).

Table S4: Electrical parameters for the model (x in cm).

Parameters	Description	Value	Ref.
C_m	Basolateral capacitance	$52.35x$ pF	based on [15]
G_m	Basolateral conductance	$64 - 49.6x$ nS	based on [15]
ϵ_3	Electromechanical coupling coefficient	$1.04 + 0.36x$ N/m/mV	based on [18]
$1/R_a^0$	apical resistance	$172\exp(-2.05x)$ nS	[3]
G_a^{max}	saturating HB conductance	Interpolated from 479 nS at x=0cm 427 nS at x=0.15cm 324 nS at x=0.224 cm 151 nS at x=0.44 cm 60 nS at x=0.67 cm 14.8 nS at x=1.12 cm	assumed
C_a	apical capacitance	50 nF/m	based on [19]
R_{tl}	resistance from ST to ground	4 Ωm	based on [20]
R_{vm}	resistance from SV to SM	25 Ωm	based on [20]
R_{vl}	resistance from SV to ground	10 Ωm	based on [20]
P_0^s	resting probability	0.4	[3]
ΔV_{hb}^0	resting value of potential difference between scala media and intracellular OHC potential	$150 - 10x$ mV	[3]

A.3 Decomposition into forward and reverse wave components

To make sure that the two forward and reverse wave components, $P_{as}^{DP,f}$ and $P_{as}^{DP,r}$, satisfy the boundary condition at the stapes, we used the following approach. At the base, the pressure is approximately 1D such that it only depends on x; the y and z dependence of the pressure can be omitted. Eq. 11 does not specify the values of the Fourier transform of $P_{as}^{DP,f}$ and $P_{as}^{DP,r}$ at $k = 0$. To find these values, the value of $\tilde{P}_{as}^{DP,f}(k = 0)$ and $\tilde{P}_{as}^{DP,r}(k = 0)$ are assumed to be given by:

$$\tilde{P}_{as}^{DP,f}(k = 0) = \alpha_P \tilde{P}_{as}^{DP}(k = 0) \tag{S6}$$

$$\tilde{P}_{as}^{DP,r}(k = 0) = (1 - \alpha_P)\tilde{P}_{as}^{DP}(k = 0) \tag{S7}$$

where α_P is a complex number. At the stapes, the forward and reverse waves should satisfy:

$$R_{st} = \frac{P_{as}^{DP,f}(x = 0)}{P_{as}^{DP,r}(x = 0)} \tag{S8}$$

Using the definition for the discrete Fourier transform:

$$\begin{aligned} P_{as}^{DP,f}(x = 0) &= \frac{1}{N}\sum_{I=1}^{N} \tilde{P}_{as}^{DP,f}(k_I) \\ &= \frac{1}{N}\Big[\alpha \tilde{P}_{as}^{DP}(k = 0) + \sum_{k>0} \tilde{P}_{as}^{DP,f}(k)\Big] \end{aligned} \tag{S9}$$

and

$$\begin{aligned} P_{as}^{DP,r}(x = 0) &= \frac{1}{N}\sum_{I=1}^{N} \tilde{P}_{as}^{DP,r}(k_I) \\ &= \frac{1}{N}\Big[(1 - \alpha_P)\tilde{P}_{as}^{DP}(k = 0) + \sum_{k<0} \tilde{P}_{as}^{DP,r}(k)\Big], \end{aligned} \tag{S10}$$

where N is the number of samples. Eq. S8 is solved for α_P to yield:

$$\alpha_P = \frac{\Big[\tilde{P}_{as}^{DP}(k = 0) + \sum\limits_{k<0} \tilde{P}_{as}^{DP}(k)\Big]R_{st} - \sum\limits_{k>0} \tilde{P}_{as}^{DP}(k)}{(1 + R_{st})\tilde{P}_{as}^{DP}(k = 0)}. \tag{S11}$$

From here, all parameters are known and the forward and reverse waves are calculated using Eqs. 9 and 10. This same procedure can be applied to the BM velocity to find its forward and reverse wave components. The BM velocity is decomposed into forward and reverse component, $v_{bm}^{DP,f}$ and $v_{bm}^{DP,r}$. The value of $\tilde{v}_{bm}^{DP,f}(k = 0)$ and $\tilde{v}_{bm}^{DP,r}(k = 0)$ are assumed to be given by:

$$\tilde{v}_{bm}^{DP,f}(k = 0) = \alpha_{bm} \tilde{v}_{bm}^{DP}(k = 0) \tag{S12}$$

$$\tilde{v}_{bm}^{DP,r}(k = 0) = (1 - \alpha_{bm})\tilde{v}_{bm}^{DP}(k = 0) \tag{S13}$$

where α_{bm} is a complex number. Satisfaction of the boundary conditions at x=0 requires that:

$$\alpha_{bm} = \frac{R_{st}\Big[\tilde{v}_{bm}^{DP}(k = 0) + \sum\limits_{k<0} \tilde{v}_{bm}^{DP}(k)\Big] - \sum\limits_{k>0} \tilde{v}_{bm}^{DP}(k)}{(1 + R_{st})\tilde{v}_{bm}^{DP}(k = 0)}. \tag{S14}$$

B Supplemental results

B.1 Fluid Mode Convergence

A convergence study was performed to determine the number of fluid modes needed to accurately capture the 3D nature of the fluid. The effect of the number of modes included on the pressure magnitude at the 20 kHz BP is shown in Fig. S3. For this convergence study, the results for the model with 75 fluid modes was used as the reference. In Fig. S3A, while there is significant variation in the magnitude for 1, 3, and 8 modes at $y = 0$, for 25 modes the results matches very closely with the results for 75 modes. The relative percent error of the fluid pressure shown in Fig. S3B is given by:

$$E_i = \left| \frac{P_{T,75} - P_{T,i}}{P_{T,75}} \right| \times 100\% \tag{S15}$$

where $P_{T,75}$ is the complex value of the pressure at $y = 0$ for the model with 75 fluid modes, and $P_{T,i}$ is the complex value of the pressure for the model with i fluid modes. While the magnitude difference is fairly large for a model with only 1 mode, by 9 modes the pressure magnitude is within 0.1 dB of the 75 mode pressure magnitude and relative error of 1.2 percent. Although fewer modes (but more than 9) could have been used to accurately model the pressure, in this work 25 modes were used. There is a fairly significant increase in computational cost when using more fluid modes during matrix assembly; however the finite element matrices were assembled once and then loaded from a file for each simulation. Once the matrices are assembled, the number of modes has no influence on the computational time needed to solve Eq. S1 using the state-space approach we previously described in [1].

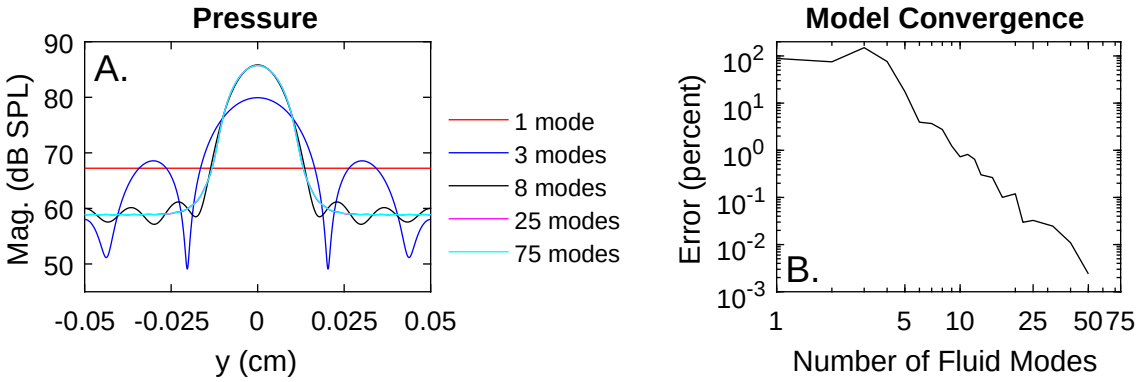

Figure S3: Convergence study for the number of fluid modes at z=0 in the SV at 20 kHz and its BP. A. Radial variations of the pressure magnitude. B. Relative percent error of the fluid pressure at y=0 relative to model with 75 pressure modes.

B.2 Comparison of model simulation for the pure tone pressure to experiments

The pure tone pressure response of the model is compared with experimental pressure measurements in two different animals [21] in Fig. S4. In Fig. S4A for the pressure 15 μm away from the BM, the model peaks in magnitude 2 dB higher than the experimental results, while in Fig. S4B, the model pressure peaks in magnitude nearly 16 dB lower than the experimental results for a 60 dB SPL stimulus. Given the variability in the experimental magnitudes, the model results for the peak magnitude are realistic. In Fig. S4, a high frequency plateau is observed in the magnitude, both for the model and the experiments; this plateau corresponds to the symmetric pressure components. The notches for the model results at 115 μm in Fig. S4A are due to interactions between the symmetric and antisymmetric pressure components. As with the BM velocity results, the model pressure phase decreases at a faster rate than the experimental results.

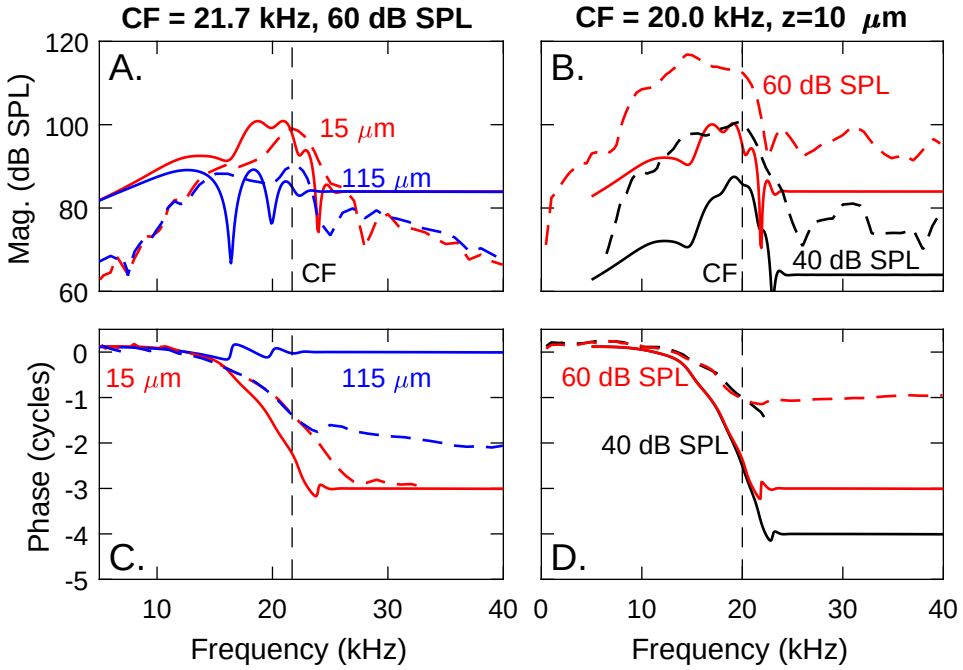

Figure S4: Comparison of fluid pressure pure tone responses for model and experimental data from [21] for 40 and 60 dB SPL stimuli. Experimental results in (A,C) and (B,D) were taken from Figs. 4 and 6, respectively, of [21]. (A-B) Magnitude. (C-D) Phase. All model phases and the experimental phases in D. are taken relative to the pressure at the stapes, while the experimental phases in C. are taken relative to the ear canal pressure. Pressures were taken at 15 and 115 μm from the BM in the ST for a 60 dB SPL stimuli (A,C) and 10 μm from the BM in the ST for 40 and 60 dB SPL stimuli (B,D). Model results are drawn with solid lines and experimental results with dashed lines.

B.3 Pure tone response at all longitudinal positions

The response of the model at all longitudinal locations is now considered with the place-frequency map, gain at CF, and quality factor shown in Fig. S5. The results in the section were obtained using a linear formulation of the model. The active model represents the response at a low stimulus level while the passive model is analogous to the response at a high stimulus level (because the feedback from outer hair cells saturates such that it has almost no effect on the acoustic response of the system at a high sound pressure level). The passive model is obtained by setting $G_{hb}^{max} = 0$ (and thus $I_{MET} = 0$). In Fig. S5A, the passive and active model place-frequency maps are compared with experimental data from [16, 17] and Greenwood's place-frequency map [22] for the gerbil cochlea. In this work, we consider the characteristic frequency (CF) to be the frequency of peak magnitude for the active linear model for a given position, which is given by the active place-frequency map. The passive model place-frequency map is in good agreement with Greenwood's map at all positions. At more basal positions, the relative frequency spacing between passive and active models for a given position matches the experimental results from [17]. At the more apical position, the frequency difference between passive and active models for a given position is larger than that of the experimental results from [16]. The gain of the BM relative to the passive model is calculated as

$$G_{bm}^{active/passive}(x) = \frac{\max\limits_{\omega} |G_{bm}^{active}(x,\omega)|}{\max\limits_{\omega} |G_{bm}^{passive}(x,\omega)|} \tag{S16}$$

where G_{bm}^{active} is the gain of the BM velocity relative to the stapes for the active model, $G_{bm}^{passive}$ is the gain of the BM velocity relative to the stapes for the passive model, and the maximum amplitude is taken across frequency for a given position. In Fig. S5B, the BM gain is plotted as a function of the CF of each location and is compared with the gain calculated from the measurements from [16, 17]. Across the range of frequencies of interest for this work, the model has at least 20 dB of gain from 7 to 40 kHz. Effort was made during the calibration process to match the experimental gain from [16, 17]. The tuning sharpness of the active model, evaluated using the quality factor, Q_{10dB}, is shown in Figure S5C. As shown in Figs. 3A and 3B, the model matches the tuning sharpness around 13 and 34 kHz best places from [16, 17]. The model has fairly broad tuning across frequency and becomes more broadly tuned towards the apex.

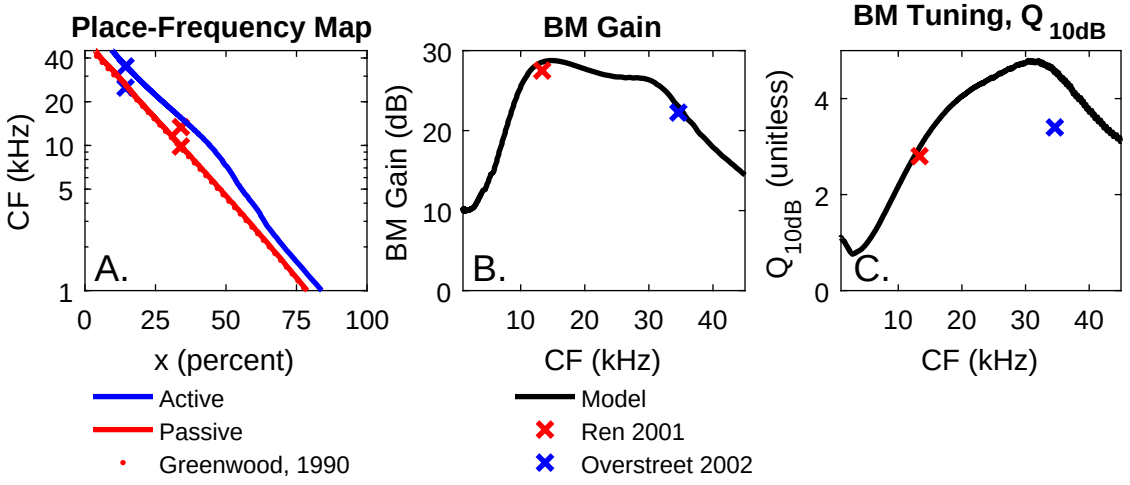

Figure S5: Comparison of BM pure tone response for model and experimental data from [22, 17, 16]. A. Place-frequency map of the passive and active models with data from [22, 17, 16]. B. Amplification of active model relative to passive model. C. Quality factor, Q_{10dB}, of the tuning of the BM. Model results are compared with measurements from the 13 kHz [16] and 34 kHz [17] best places.

B.4 Variations on Pressure with Distance from the BM

The spatial variations of the fluid pressure of the primary tones and DP obtained with the model are compared with pressure measurements by Dong and Olson [24] in Fig. S6. For these measurements, the primary frequencies were varied so that f_2, f_1, and f_{DP} were alternatively set to CF = 21 kHz. In all three cases, both model and experimental primaries show very little spatial variation. The DP decreases at a fast rate as the distance from the BM increases, both in the model simulations and the experiments; however, the slope seen in the model simulations is steeper than in the measurements. When the DPs from Fig. S6A-C are compared to a low intensity pure tone of the same frequency (Figs. S6D-F), similar decreases in magnitude with distance from the BM are found, which has also been observed experimentally (see Fig. 4B in [21]). However, the pure tone pressure converges to a higher value than the DP pressure at large distances from the BM because the pure tone symmetric pressure is higher than the DP symmetric pressure (Figs. S6G-I). The pure tone and DP antisymmetric pressure decrease at nearly the same rate and converge to approximately the same value. For all three cases, the antisymmetric pressure is much higher than the symmetric pressure close to the BM and decreases exponentially with increasing distance from the BM. Close to the BM, the antisymmetric pressure dominates the symmetric pressure, while farther from the BM the symmetric pressure dominates the antisymmetric pressure, at which point the total pressure varies little with distance from the BM.

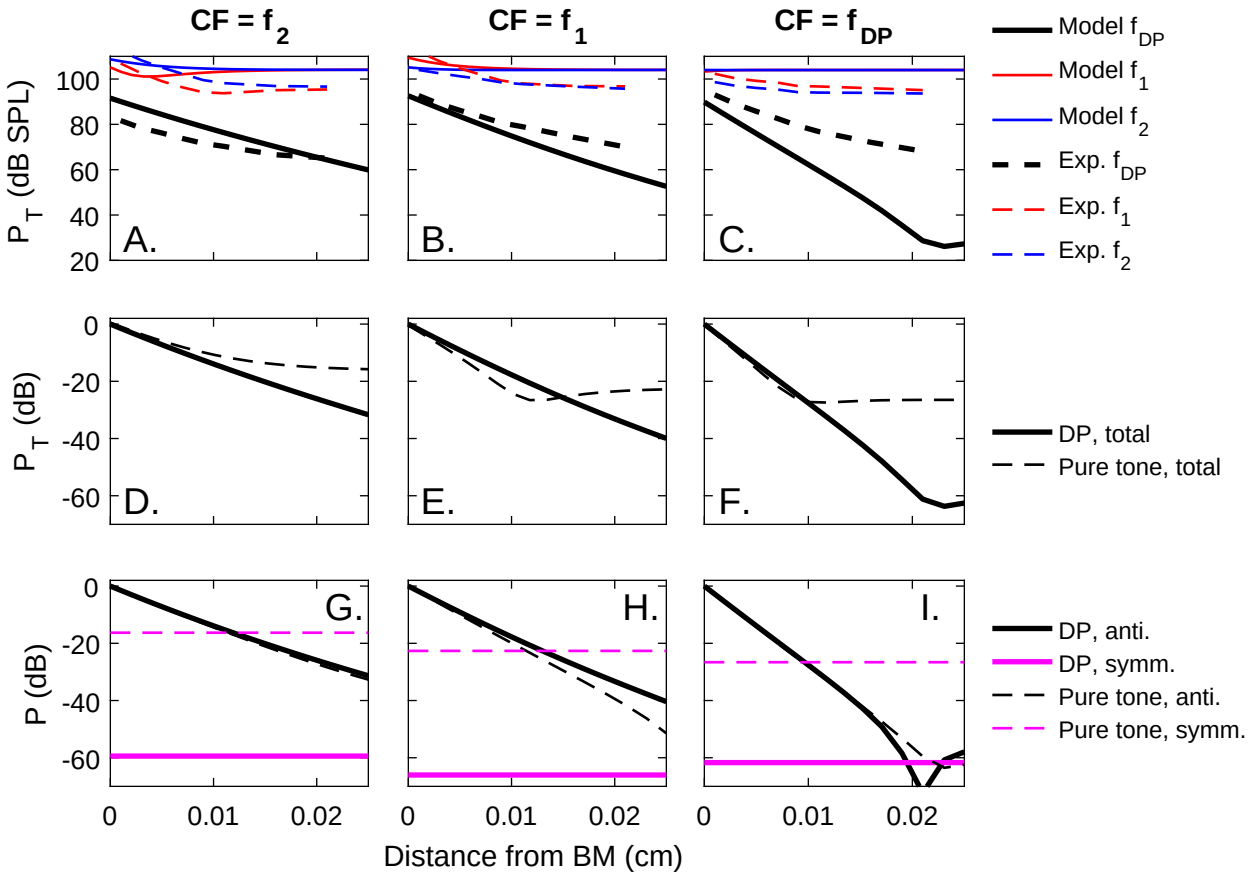

Figure S6: A-C. Comparison of pressure magnitude vs distance from BM in ST with data from [24]. D-F. Comparison of total pressure magnitude vs distance from BM in ST for DP and pure tone of the same frequency. G-I. Decomposition of the pressure from D-F into symmetric and antisymmetric components. Horizontal lines in G-I are the symmetric pressures. All model and experimental data were taken at the 21 kHz best place with primary stimuli of 80 dB SPL and f_2/f_1=1.10. The pure tone model results in D-I were obtained from the nonlinear model with a stimulus at 30 dB SPL. Magnitudes in D-I were normalized by the magnitude of the antisymmetric pressure at the BM, $P_{as}(z = 0)$.

B.5 Effect of Varying Primary Stimulus Level

Nonlinear two-tone simulations for different primary stimuli levels are compared with experimental measurements taken by [21]. For both the 50 dB SPL model and experimental results the magnitude peaks near f_{DP}=CF, while for 80 dB SPL the model peaks near f_{DP}=CF and the experimental results peak at a slightly lower frequency (f_2=27 kHz). Both 50 and 80 dB SPL model results show a notch in magnitude and corresponding phase shift below 20 kHz; the notch and phase shift are due to the interference between the forward and reverse waves. Below this phase shift, the phase is either nearly flat or has a slight positive slope indicating a reverse wave.

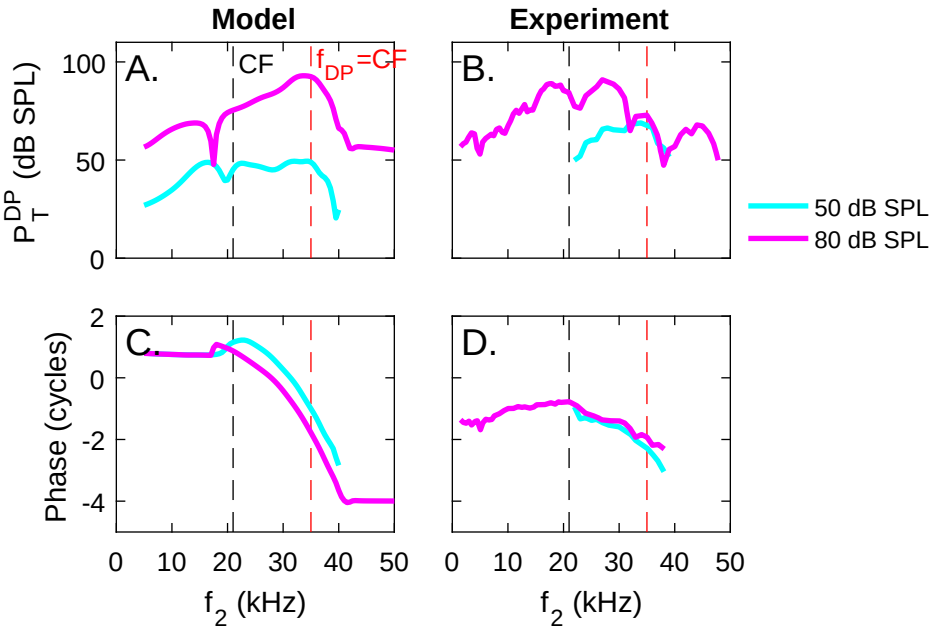

Figure S7: DP model and experimental measurements from [21] of fluid pressure for varied stimulus levels. Model results and experimental measurements were taken at 21 kHz BP in ST 10 μm from BM for f_2/f_1=1.25. The model phase is referenced to the pressure in the SV at the stapes and the experimental phase is taken relative to the ear canal pressure. A.,B. Magnitude of fluid pressure. C.,D. phase of fluid pressure.

B.6 Effect of Primary Frequency Ratio on Forward and Reverse Waves

The effect of varying the primary frequency ratio on the forward and reverse waves is shown in Fig. S8.

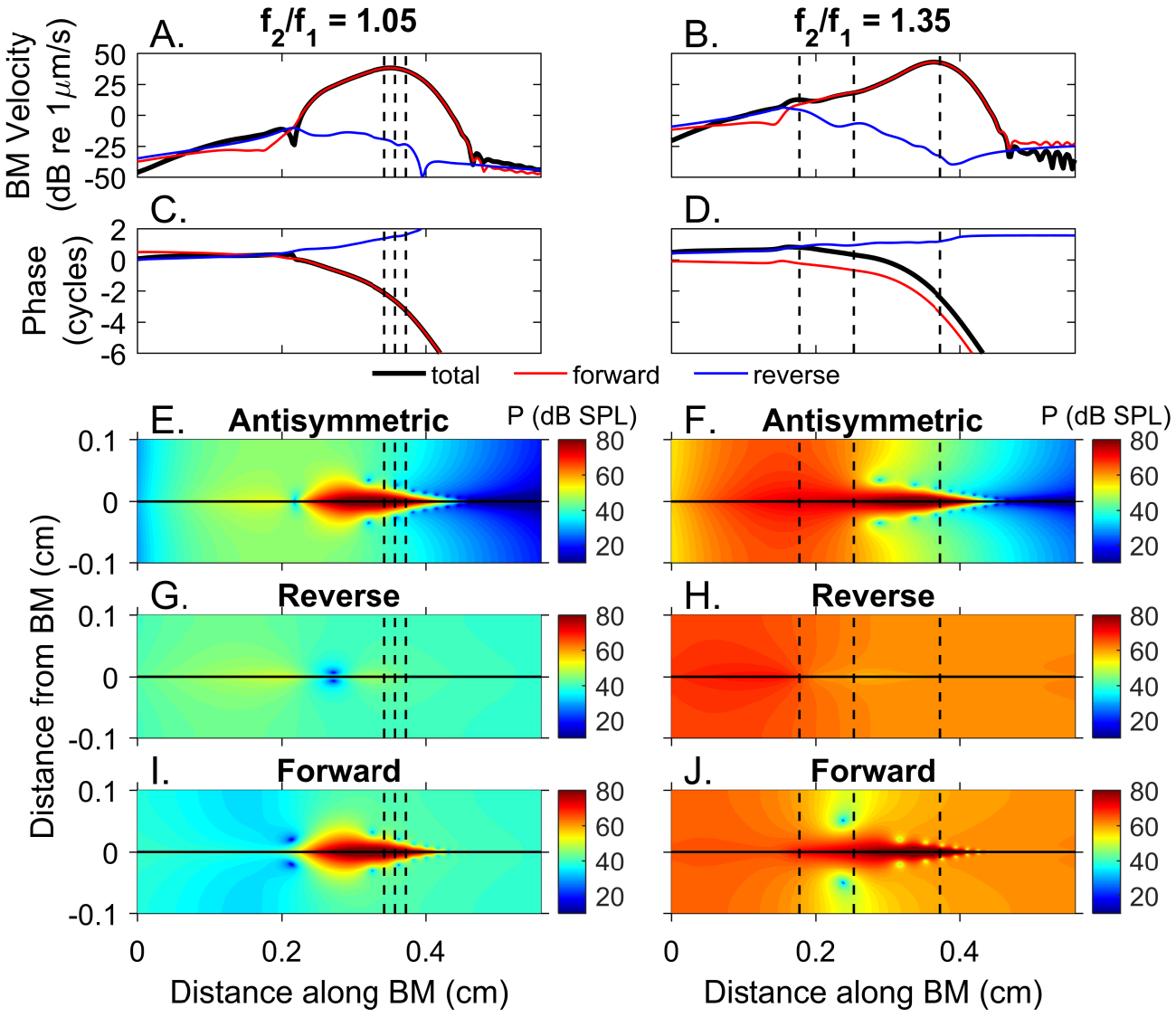

Figure S8: Decomposition of BM velocity and antisymmetric pressure at f_{DP} into forward and reverse waves for equi-level primaries of 80 dB SPL for $f_2/f_1 = 1.05$ and 1.35, and f_{DP}=16 kHz. A.,B. Magnitude of BM velocity. C.,D. Phase of BM velocity. E.,F. Magnitude of antisymmetric pressure. G.,H. Magnitude of reverse wave component of antisymmetric pressure. I.,J. Magnitude of forward wave component of antisymmetric pressure. The vertical dashed lines indicate, from left to right, the f_2, f_1, and f_{DP} best places.

B.7 Effect of Stapes Reflection on Forward and Reverse Waves

To investigate the role of the middle ear on DP propagation, two additional middle ear models were developed (see Table S3 and Fig. S2) (1) with a stapes reflection coefficient, R_{st}, of high magnitude across frequency and (2) with a stapes reflection coefficient of small magnitude at 16 kHz. The high $|R_{st}|$ is the case when most energy propagating in the reverse direction is reflected back into the cochlea, while for the low $|R_{st}|$ case very little of the reverse wave for f_{DP} is reflected back into the cochlea.

The effect of varying the stapes reflection coefficient is investigated in Fig. S9. The most predominant changes in varying the stapes occur in the most basal regions, while closer to the DP best place the effect of the stapes variations appears negligible. For the high $|R_{st}|$ model, the forward and reverse waves have approximately the same magnitude while the phase differs by half a cycle (due to the phase of R_{st}). As a result of this phase difference, the total BM velocity and antisymmetric pressure close to the stapes is relatively small. For the low $|R_{st}|$ case, very little of the reverse wave is reflected at the stapes and thus the forward wave is very small at the stapes.

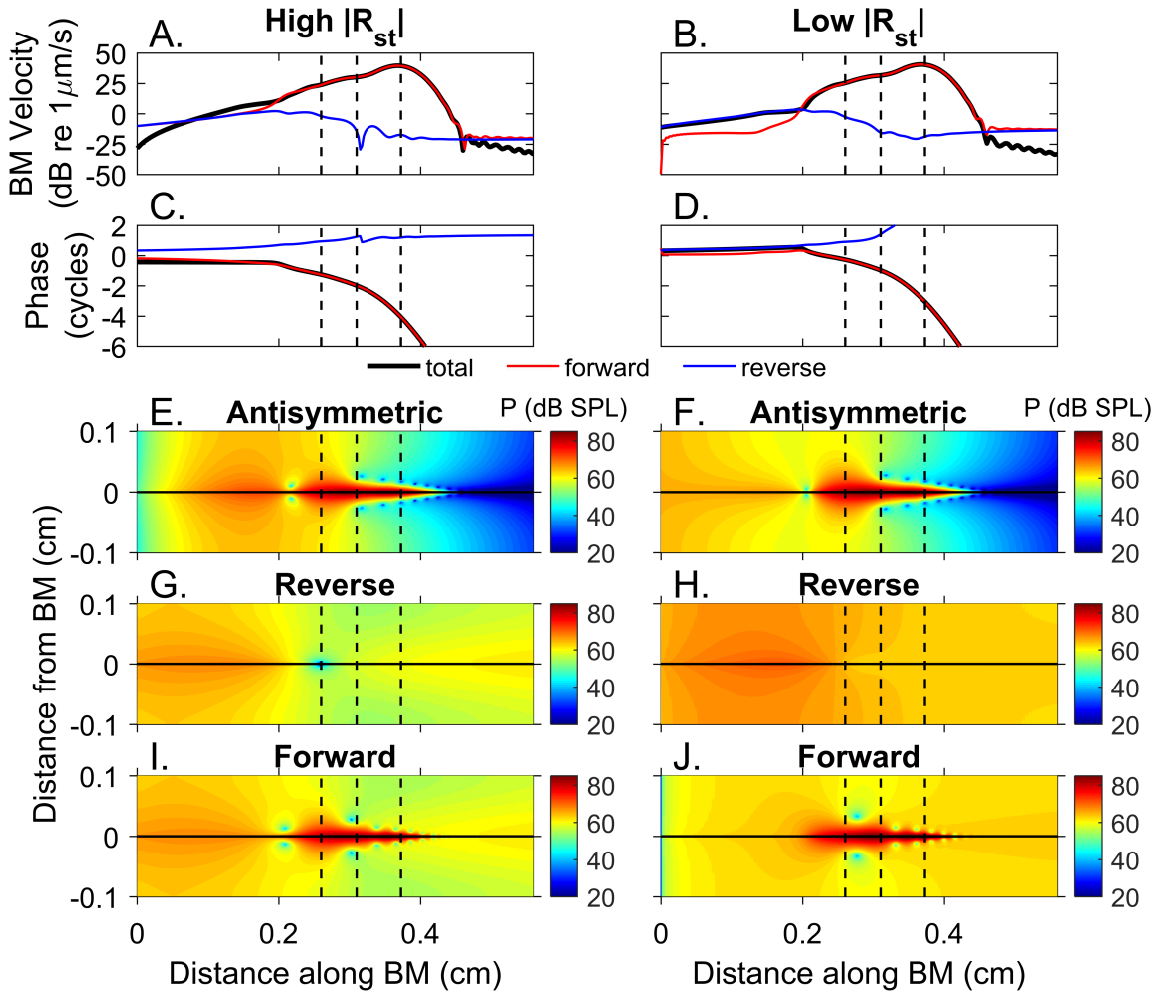

Figure S9: Decomposition of BM velocity and antisymmetric pressure at f_{DP} into forward and reverse waves for equi-level primaries of 80 dB SPL with $f_2/f_1 = 1.20$ and f_{DP}=16 kHz for different middle ear models. A.,B. Magnitude of BM velocity. C.,D. Phase of BM velocity. E.,F. Magnitude of antisymmetric pressure. G.,H. Magnitude of reverse wave component of antisymmetric pressure. I.,J. Magnitude of forward wave component of antisymmetric pressure. The vertical dashed lines indicate, from left to right, the f_2, f_1, and f_{DP} best places.

B.8 Movies

Movie S1. Movie of the steady state DP fluid pressure for equi-level primaries of 80 dB SPL with f_2/f_1=1.20 and f_2 = 24 kHz with the baseline middle ear model. All pressure components are normalized by the maximum total pressure value. Because most of the pressure amplitudes are much smaller than the maximum normalized pressure of 1, the colorbar limits were set to a smaller value (-0.05 to 0.05) to highlight the spatial variations of the pressure. The waveform shows the normalized total pressure at the stapes in the center of the SV.

Movie S2. Movie of the steady state DP fluid pressure for equi-level primaries of 80 dB SPL with f_2/f_1=1.20 and f_2 = 24 kHz with the Low $|R_{st}|$ middle ear model. All pressure components are normalized by the maximum total pressure value. Because most of the pressure amplitudes are much smaller than the maximum normalized pressure of 1, the colorbar limits of the pressure were set to a smaller value (-0.05 to 0.05) to highlight the spatial variations of the pressure. The waveform shows the normalized total pressure at the stapes in the center of the SV.

Supporting References

[1] Meaud, J. and C. Lemons. 2015. Nonlinear response to a click in a time-domain model of the mammalian ear. *J. Acoust. Soc. Am.* 138:193–207.

[2] Ramamoorthy, S., N. V. Deo, and K. Grosh. 2007. A mechano-electro-acoustical model for the cochlea: response to acoustic stimuli. *J. Acoust. Soc. Am.* 121:2758–2773.

[3] Meaud, J. and K. Grosh. 2012. Response to a pure tone in a nonlinear mechanical-electrical-acoustical model of the cochlea. *Biophys. J.* 102:1237–1246.

[4] Edge, R. M., B. N. Evans, M. Pearce, C.-P Richter, X. Hu, and P. Dallos. 1998. Morphology of the unfixed cochlea. *Hear. Res.* 124:1–16.

[5] Meaud, J. and K. Grosh. 2010. The effect of tectorial membrane and basilar membrane longitudinal coupling in cochlear mechanics. *J. Acoust. Soc. Am.* 127:1411–1421.

[6] Fernández, C. 1952. Dimensions of the cochlea (guinea pig). *J. Acoust. Soc. Am.* 24:519–523.

[7] Richter, C.-P., R. Edge, D. Z. Z. He, and P. Dallow. 2000. Development of the gerbil inner ear observed in the hemicochlea. *J. Assoc. Res. Otolaryngol.* 1:195–210.

[8] Richter, C.-P., G. Emadi, G. Getnick, A. Quesnel, and P. Dallos. 2007. Tectorial membrane stiffness gradients. *Biophys. J.* 93:2265–2276.

[9] Meaud, J., and K. Grosh. 2014. Effect of the attachment of the tectorial membrane on cochlear micromechanics and two-tone suppression. *Biophys. J.* 106:1398–1405.

[10] Ghaffari, R., A. J. Aranyosi, and D. M. Freeman. 2007. Longitudinally propagating traveling waves of the mammalian tectorial membrane. *Proc. Natl. Acad. Sci. U.S.A.* 104:16510–16515.

[11] Puria, S. 2003. Measurements of human middle ear forward and reverse acoustics: implications for otoacoustic emissions. *J. Acoust. Soc. Am.* 113:2773–2789.

[12] Shera, C. A. and G. Zweig. 1991. Reflection of retrograde waves within the cochlea and at the stapes. *J. Acoust. Soc. Am.* 89:1290–1305.

[13] de La Rochefoucauld, O., W. F. Decraemer, S. M. Khanna, and E. S. Olson. 2008. Simultaneous measurements of ossicular velocity and intracochlear pressure leading to the cochlear input impedance in gerbil. *J. Assoc. Res. Otolaryngol.* 9:161–177.

[14] Overstreet III, E. H. and M. A. Ruggero. 2002. Development of wide-band middle ear transmission in the Mongolian gerbil. *J. Acoust. Soc. Am.* 111:261–270.

[15] Johnson, S. L., M. Beurg, W. Marcotti, and R. Fettiplace. 2011. Prestin-driven cochlear amplification is not limited by the outer hair cell membrane time constant. *Neuron.* 70:1143–1154.

[16] T. Ren and A. L. Nuttall. 2001. Basilar membrane vibration in the basal turn of the sensitive gerbil cochlea. *Hear. Res.* 151:48–60.

[17] Overstreet III, E. H., A. N. Temchin, and M. A. Ruggero. 2002. Basilar membrane vibrations near the round window of the gerbil cochlea. *J. Assoc. Res. Otolaryngol.* 3:351–361.

[18] Iwasa, K. H. and M. Adachi. 1997. Force generation in the outer hair cell of the cochlea. *Biophys. J.* 73:546–555.

[19] Dallos, P. and B. N. Evans. 1995. High-frequency motility of outer hair cells and the cochlear amplifier. *Science.* 267:2006.

[20] Strelioff, D. 1973. A computer simulation of the generation and distribution of cochlear potentials. *J. Acoust. Soc. Am.* 54:620–629.

[21] Dong, W. 2017. Simultaneous intracochlear pressure measurements from two cochlear locations: Propagation of distortion products in gerbil. *J. Assoc. Res. Otolaryngol.* 18:209–225.

[22] Greenwood, D. D. 1990. A cochlear frequency-position function for several species? 29 years later. *J. Acoust. Soc. Am.* 87:2592–2605.

[23] Dong, W. and E. S. Olson. 2013. Detection of cochlear amplification and its activation. *Biophys. J.* 105:1067–1078.

[24] Dong, W. and E. S. Olson. 2005. Two-tone distortion in intracochlear pressure. *J. Acoust. Soc. Am.* 117:2999–3015.